6

Application to the Biaxial Fragmentation of Shells

Much of the development of a statistical energy-based theory of fragmentation of stretching ductile metals has been restricted to one-dimensional geometries such as expanding rings or, at best, a uniformly expanding cylinder where the theory is intended to describe the average and statistical spacing of axial fractures. In this chapter an analysis will be extended to describe the breakup of a biaxial expanding shell or membrane of ductile metal in which stretching rates in mutually orthogonal directions are each nonzero and are, in general, different. A specific case of interest, of course, is that of a stretching spherical shell segment in which the orthogonal stretching rates are the same.

In the development of the present two-dimensional fragmentation theory it will be assumed that at a point on the surface of the expanding shell orthogonal principal stretching directions can be determined and that fracture in the two principle directions are independent and governed by the conditions of the linear fragmentation theory developed in the earlier sections. This approach is illustrated in Fig. 6.1, where principal stretching directions on a surface are identified and a corresponding statistical distribution of fractures along the x and y stretching directions partition the surface into a statistical distribution of fragment areas.

6.1 The Fragment Size and Aspect Ratio Scales

Within the energy governed region of the linear statistical fragmentation theory a fracture activation rate, and a corresponding fracture spacing length scale, has been determined in the previous chapter based on a property of the material identified as the fragmentation toughness and the rate of stretching leading to fracture. The same relation will be used to determine the fracture spacing length scale in both orthogonal principal stretching directions. Namely,

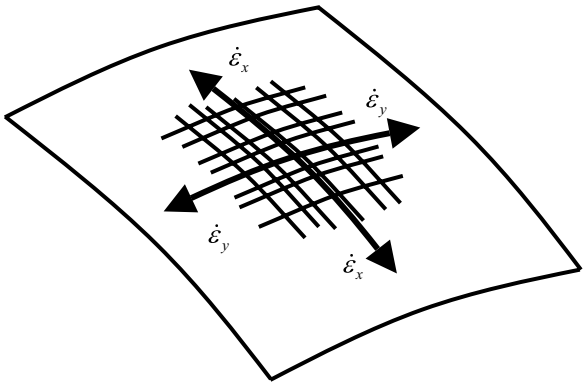

Fig. 6.1. Illustrates independent application of linear statistical fragmentation theory in orthogonal principal stretching directions to implement fragmentation of the surface at a point

$$x_o = \left(\frac{\sqrt{12} K_f}{\rho c \dot{\varepsilon}_x} \right)^{2/3} , \tag{6.1}$$

and,

$$y_o = \left(\frac{\sqrt{12} K_f}{\rho c \dot{\varepsilon}_y} \right)^{2/3} . \tag{6.2}$$

The fragment area scale is then determined from,

$$a_o = x_o y_o = \left(\frac{\sqrt{12} K_f}{\rho c \bar{\dot{\varepsilon}}} \right)^{4/3} , \tag{6.3}$$

where,

$$\bar{\dot{\varepsilon}} = \sqrt{\dot{\varepsilon}_x \dot{\varepsilon}_y} \, . \tag{6.4}$$

The nominal fragment aspect ratio is provided by,

$$r_o = x_o / y_o = \left(\dot{\varepsilon}_x / \dot{\varepsilon}_y \right)^{-2/3} . \tag{6.5}$$

Predictions of the fragment area scale based on (6.3) as a function of the stretching rate are shown in Fig. 6.2. The predicted curve is based on the equiaxial explosion driven expansion and fragmentation of a spherical shell segment of a common metal. The experimentally observed fracture fabric was in sensible qualitative and quantitative agreement with the predicted behavior. At typical stretching rates of a few times 10^3/s up to about 10^4/s for explosively loaded metal shells a fragment size scale on the order of a square centimeter or less, is predicted consistent with experimental observation. Increasing strain rate decreases this size scale. Increased toughness, on the other hand, is predicted to increase fragment size.

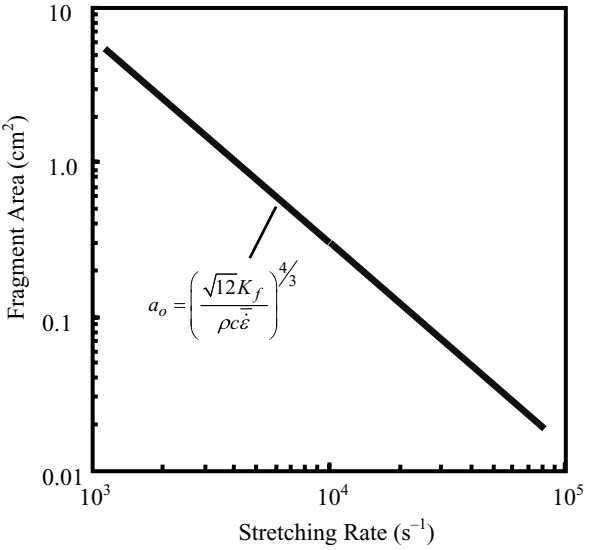

Fig. 6.2. Fragment area scale versus mean stretching rate based on energy determined characteristic fracture spacing and properties for equiaxial expansion of a metal

6.2 The Biaxial Fragment Distribution Properties

The dynamic fragmentation of a rapidly stretching metal shell involves a complexity of rapidly opening fissures and cracks that result in a multiplicity of separate fragments. Individual fragments continue on outward divergent paths at the velocity at which breakup occurred. Although the size scale determined previously adequately characterizes the number density and average size of these fragments, a statistical distribution in fragment size is clearly observed. The objective here will be to apply the linear statistical fragmentation theory to characterize the distribution in area fragment size observed experimentally.

In the linear theory, based on the Mott statistical premise, as constrained by the energy-based fracture spacing, a statistical distribution in fracture spacing was determined. The resulting distribution was found to satisfactorily describe linear fragmentation experiments such as the expanding ring studies. In the present development the assumption of independent statistical fracture in mutually orthogonal principal stretching directions is continued. The statistical size distribution to be pursued is as illustrated in Fig. 6.3. In either the x direction, or in the orthogonal y direction, the statistical spacing of fractures (lines) is governed by the linear Mott statistical distribution with independent length scales of x_o and y_o provided through (6.1) and (6.2), respectively. The statistical distribution in spacing in the x direction derived previously is,

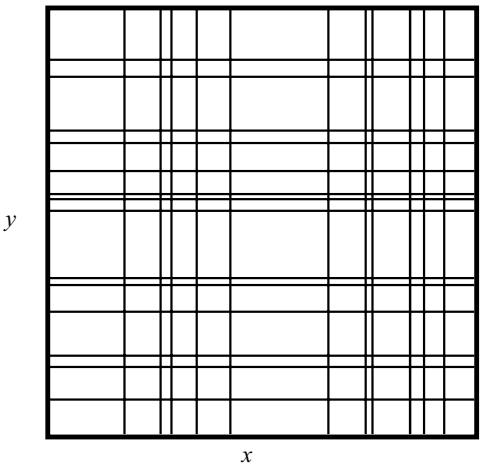

Fig. 6.3. Illustrates independent statistical distributions of fracture spacing in orthogonal x and y principal stretching directions. Areas determined by intersecting lines will model statistical distribution in fragment areas and fragment aspect rations

$$f\,(x) = \frac{\beta^2}{4}\frac{1}{x_o}\left(\frac{x}{x_o}\right)^3 e^{-\frac{1}{4}(x/x_o)^3}\int_0^1 \left(1-y^2\right) e^{-\frac{3}{4}(x/x_o)^3 y^2} dy\ , \tag{6.6}$$

where, $\beta = 3/\Gamma(2/3)$. An equivalent distribution applies to the spacing distribution in the y direction. With further analytic manipulation the integral in (6.6) can be expressed as an error function, if useful. The careful reader will note that the length scale x_0 in (6.6) is not precisely the expected value of the fragment size (see (3.121)). Uncertainties resulting from the assumptions leading to (6.1) and (6.2) provide allowance for this lack of rigor.

6.2.1 Fragment Area Distribution

The linear Mott distribution provided by (6.6) is not convenient for an analytic determination of the distribution in fragment areas provided by the overlap of horizontal and vertical lines as illustrated in Fig. 6.3. The approach pursued here will be to approximate the distribution from (6.6) with another more analytically tractable distribution. The distributions that will be tried are the Weibull distribution,

$$f(x) = \frac{n}{x_o}\left(\frac{x}{x_o}\right)^{n-1} e^{-(x/x_o)^n}\ , \tag{6.7}$$

and the gamma distribution,

$$f(x) = \frac{1}{x_o}\frac{n}{\Gamma(n)}\left(\frac{nx}{x_o}\right)^{n-1} e^{-nx/x_o}\ . \tag{6.8}$$

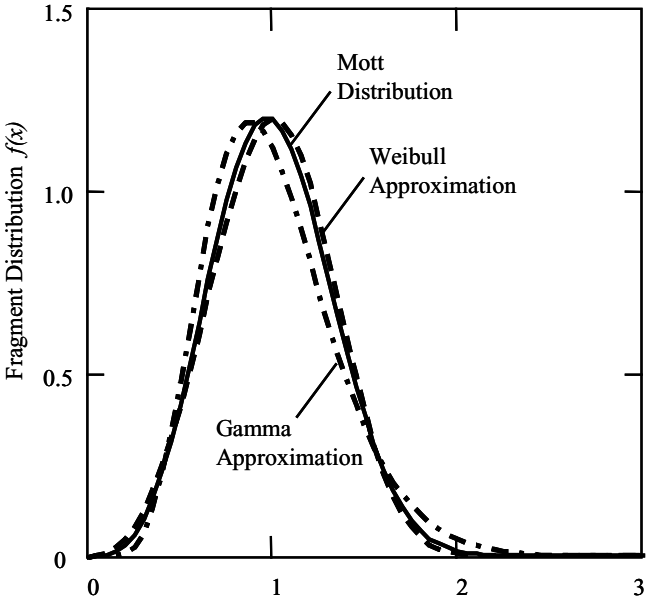

Fig. 6.4. Mott linear fragment size distribution compared with Weibull and Gamma distribution approximations

The Weibull and gamma distributions with the distribution parameter n adjusted to provide the optimum fit to the Mott distribution are compared with the Mott distribution from (6.6) in Fig. 6.4. Values of $n = 3.45$ for the Weibull distribution and $n = 8.0$ for the gamma distribution yielded the observed results. The Weibull distribution clearly provides the closer fit to the desired Mott distribution. Both Weibull and gamma distributions will be carried through the analysis in developing a fragment area distribution. Both are analytically tractable and both solutions provide a measure of sensitivity to the fit between the Mott distribution in (6.6) and either of the approximations in (6.7) and (6.8).

Working first with the Weibull distribution, an expression assessing the two-dimensional statistical partitioning of the surface in Fig. 6.3 is immediately written as a juxtaposition of (6.7) and the corresponding distribution in the y direction. Namely,

$$f(x,y) = \frac{n^2}{x_o y_o}\left(\frac{xy}{x_o y_o}\right)^{n-1} e^{-(x/x_o)^n} e^{-(y/y_o)^n} , \tag{6.9}$$

provides the probability density distribution for fragment areas of length x and width y. Equation (6.9) can be transformed to distribution over fragment area,

$$a = xy , \tag{6.10}$$

and aspect ratio,

$$r = x/y \; . \tag{6.11}$$

The differential invariant,

$$f(x,y)dxdy = g(a,r)\,dadr \; , \tag{6.12}$$

leads to,

$$dxdy = \left|\frac{\partial(x,y)}{\partial(a,r)}\right| dadr \; , \tag{6.13}$$

for the differential element through the transformation Jacobian [Buck, 1965]. Accordingly, the transformed probability density function is,

$$g(a,r) = f(x(a,r), y(a,r)) \left|\frac{\partial(x,y)}{\partial(a,r)}\right| \; . \tag{6.14}$$

Calculating the Jacobian through (6.10) and (6.11),

$$\left|\frac{\partial(x,y)}{\partial(a,r)}\right| = \frac{1}{2r} \; , \tag{6.15}$$

yields,

$$g(a,r) = \frac{1}{2}\frac{n^2}{(x_o y_o)^n}\frac{a^{n-1}}{r} e^{-\left(\frac{1}{x_o}\sqrt{ar}\right)^n} e^{-\left(\frac{1}{y_o}\sqrt{a/r}\right)^n} \; . \tag{6.16}$$

The distribution over fragment area is then written as the integral expression,

$$h(a) = \frac{n^2}{2a_o}\left(\frac{a}{a_o}\right)^{n-1} \int_0^\infty \frac{1}{r} e^{-\left(\sqrt{a/a_o}\right)^n \left[(r/r_o)^{n/2} + (r/r_o)^{-n/2}\right]} dr \; , \tag{6.17}$$

where, $a_o = x_o y_o$ and $r_o = x_o/y_o$. The substitution,

$$r = r_o e^{2\eta/n} \; , \tag{6.18}$$

provides,

$$h(a) = \frac{2n}{a_o}\left(\frac{a}{a_o}\right)^{n-1} \int_0^\infty e^{-2\left(\sqrt{a/a_o}\right)^n \cosh\eta} d\eta \; . \tag{6.19}$$

The integral is a modified Bessel function [Abramowitz and Stegun, 1954] yielding, for the area distribution, based on a Weibull approximation for the linear spacing distribution,

$$h(a) = \frac{2}{a_o}\left(\frac{a}{a_o}\right)^{n-1} K_o\left(2\left(\sqrt{a/a_o}\right)^n\right) \; . \tag{6.20}$$

A similar exercise using the gamma approximation provides,

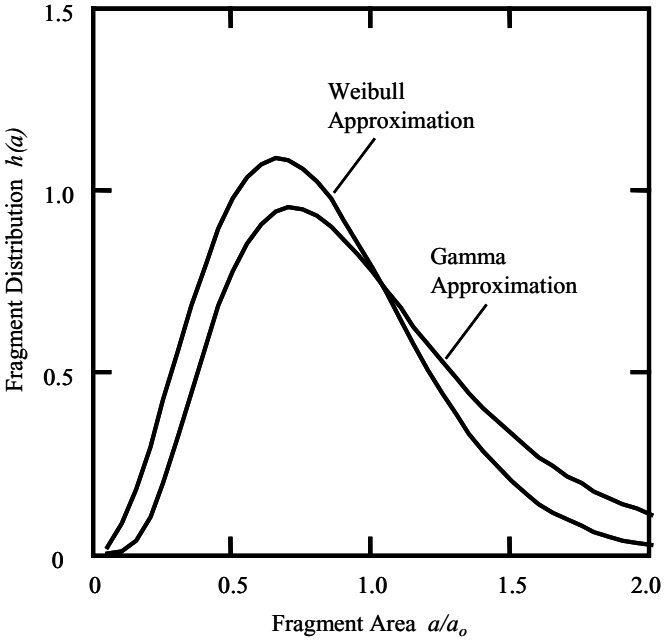

Fig. 6.5. Fragment area distributions base on Weibull and gamma distribution approximations to the Mott linear distribution

$$h(a) = \frac{2}{a_o}\left(\frac{n}{\Gamma(n)}\right)^2\left(\frac{n^2 a}{a_o}\right)^{n-1} K_o\left(2n\sqrt{a/a_o}\right) \ . \tag{6.21}$$

Area distributions resulting from the Weibull and the gamma distribution approximations to the linear Mott statistical fracture spacing distribution are shown in Fig. 6.5. The Weibull approximation provides a noticeably better fit to the linear distribution in Fig. 6.4 and is expected to provide the better representation of the area distribution based on the Mott theory.

Comparison of the Weibull approximation to the Mott area distribution based on random line partitioning of the area is compared with experimental results from the dynamic near-spherical expansion fragmentation of a metal shell in Fig. 6.6. The theoretical distribution reasonably represents the measured experimental distribution.

6.2.2 Fragment Linear Size Distribution

It is common in the experimental analysis and display of radiographic data of fragmentation of expanding metal surfaces to express the distribution in terms of a characteristic linear fragment size. For example, we will here identify the fragment size $s = a^{1/2}$, where a is the previous fragment area defined above.

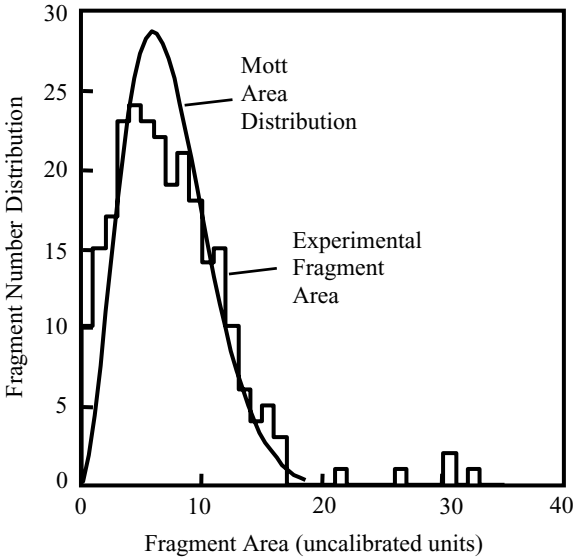

Fig. 6.6. A comparison of the theoretical distribution for fragment areas with experimental results

The statistical distribution in fragment size s is a straightforward transformation of the area distributions provided above. For completeness the appropriate statistical size distributions and their pictorial representation will be provided here. The appropriate transformation for (6.20), based on the Weibull approximation to the linear Mott distribution, leads to,

$$h(s) = \frac{4n}{s_o}\left(\frac{s}{s_o}\right)^{2n-1} K_o\left(2(s/s_o)^n\right) \ , \tag{6.22}$$

for the statistical size distribution. In contrast, (6.21) based on the gamma approximation provides,

$$h(s) = \frac{4}{s_o}\left(\frac{n^n}{\Gamma(n)}\right)^2\left(\frac{s}{s_o}\right)^{2n-1} K_o\left(2n(s/s_o)\right) \ . \tag{6.23}$$

Both size distributions are shown and compared in Fig. 6.7.

6.2.3 Fragment Aspect Ratio Distribution

The analysis pursued here also lends itself to a sensible assessment of the statistical distribution in fragment aspect ratio. Working with the distribution provided by the Weibull representation of the Mott distribution as written in (6.16), substitute the parameters $r_o = x_o/y_o$, $\xi = a/a_o$ and $\rho = r/r_o$. Integration over the fragment area variable is then written,

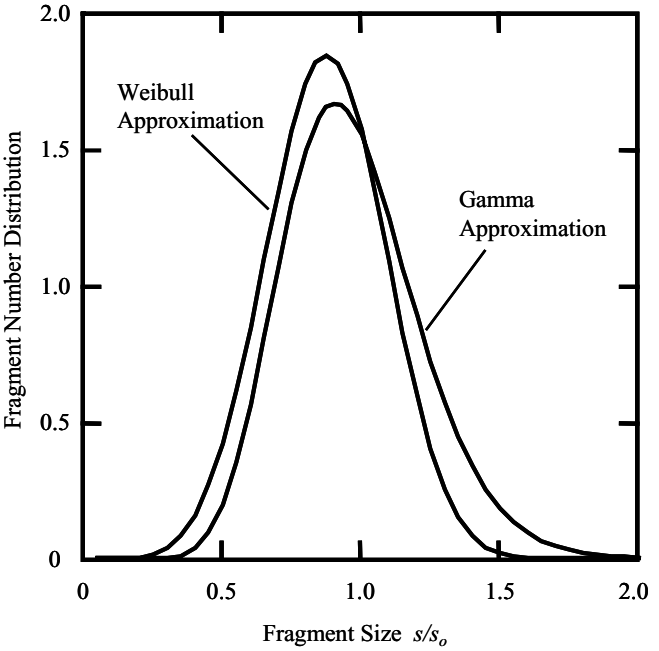

Fig. 6.7. Fragment size distributions base on Weibull and gamma distribution approximations to the Mott linear distribution

$$k(r) = \frac{1}{2}\frac{n^2}{r_o}\frac{1}{\rho}\int_0^\infty \xi^{n-1} e^{-(\rho^{n/2}+\rho^{-n/2})\xi^{n/2}} d\xi \ . \tag{6.24}$$

Equation (6.24) is readily integrated providing,

$$k(r) = \frac{n}{r_o}\frac{\rho^{n-1}}{(1+\rho^n)^2} \ . \tag{6.25}$$

The distribution over fragment aspect ratio with $n = 3.45$ is shown in Fig. 6.8. A similar distribution can be derived for the gamma distribution approximation to the Mott distribution.

6.3 Biaxial Strain to Failure Model

Neither the statistical fragmentation theory of Mott, nor the energy-based theory of fragmentation addresses the underlying deformation that a rapidly expanding metal shell can sustain before onset of fracture. Other physical considerations must be explored in pursuing a theory of the onset of fracture leading to the statistical fragmentation accompanying the disintegration of the expanding shell.

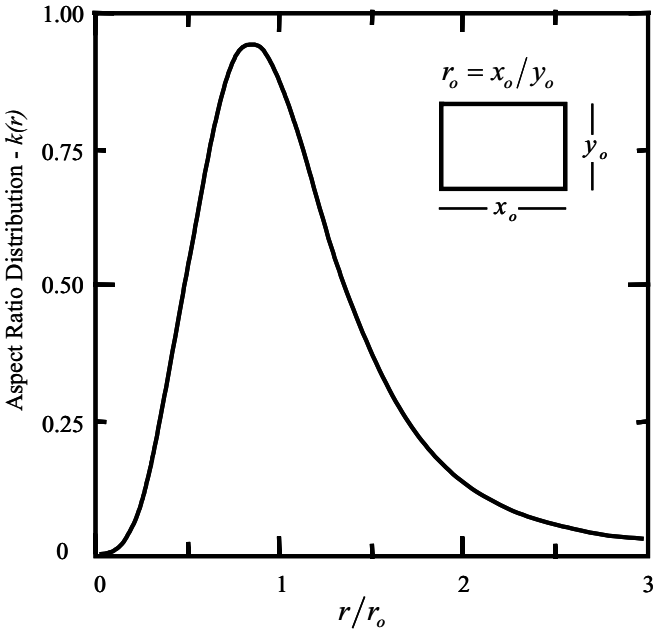

Fig. 6.8. Statistical distribution in fragment aspect ratio

As discussed earlier, Mott explored this issue on several levels. He pursued the ductile failure of steel tensile specimens in evaluating the critical gamma parameter in his relation for the prediction of fragment size. He also presaged the direction of much later work in forecasting the internal damage evolution through loss of cohesion in plastic straining metals and the dependence of this phenomenon on the local state of stress triaxiality.

The explosive impulsive load leads rapidly to the divergent plastic stretching and thinning of the metal shell. The onset of fracture is dependent on the thermo-plastic deformation properties and the geometry of the metal shell. The driving explosive pressure quickly diminishes to a negligible level and the outward divergent inertia of the body sustains the plastic deformation.

The latter comment, of course, introduces complicating considerations. The Gurney theory of explosive shell expansion [Gurney, 1943] assumes a sustained driving pressure reduced only by subsequent expansion of the accelerated shell. In energetic ideal explosives, however, much of the accelerating energy is imparted in the initial shock with rapid drop in the later driving pressure. Less ideal explosives, in contrast, will impart a larger fraction of the kinetic energy in late time push.

In any case both inertia and strain hardening of the plastic flow affect stability of the expanding and thinning shell. Sufficient inertia can lead to acceleration stresses which stabilize small perturbations in the thinning process [Romero 1991]. Inertial stabilization in this sense, however, does not appear

to play a significant role in governing the onset of fracture in the breakup of explosive driven shells.

Deformation hardening in the flow process appears paramount in stabilizing the plastic expansion and is the principal mechanism through which many materials sustain appreciable plastic deformation before rupture. The present dynamic expansion and rupture of metal shells have similarities to the extensive field of quasi-steady metal forming [e.g., Bartlat 1989]. The present application can be profitably studied through exploitation of this literature.

In essence plastic strain hardening stabilizes the thinning instabilities brought about by the reduction of in-plane tension caused by thinning of the stretching shell. While strain hardening dominates geometric softening (reduction in the tensile force due to the concomitant reduction in cross-sectional area), thinning through stable plastic expansion ensues. Saturation of strain hardening, however, ultimately leads to instability and rupture.

Plastic thinning instabilities are not unique to the dynamic environment. Within the physics introduced, namely rate independent strain hardening and geometric softening, the onset and subsequent growth of thinning instabilities would proceed the same on any time scale from static to rapid dynamic. Additional physical considerations markedly alter the dynamic event, however. These include the properties of material inertia and thermal conductivity in addition to rate sensitivity of the flow properties.

On the length scale of thinning instabilities, plastic dissipation in the dynamic event is effectively adiabatic. Plastic dissipation and the accompanying thermal softening will alter the effective stress versus strain behavior. Onset of instability would consequently occur earlier than in the corresponding static isothermal event. Adiabatic thermal softening would also localize the thinning instability growth process, markedly changing the character of the thinning and necking region. Unbounded thermal localization in the thinning region is constrained by local inertia, however.

The influence of adiabatic thermal softening on the onset of the tensile thinning instability is expected to be a second order effect. Thermal softening in the subsequent plastic flow during the growth of this instability under the appropriate loading conditions can profoundly alter the failure process, however. Along planes of maximum plastic shear (approximately 45 degrees with respect to the plane of the thinning shell) perturbations in the local temperature or deformation can lead to localized adiabatic shear deformation (adiabatic shear bands) within thin planar regions. Rupture of the expanding shell is then accommodated by the plastic shearing and separation of the body along the planes of adiabatic shear.

Adiabatic shear band failure, like fracture, is enhanced by inhomogeneities in the stress or deformation field. And also like fracture, adiabatic shear bands have a propensity for propagating from a site of initiation through the plane of shear rather than evolving homogeneously throughout that plane. Thus, shear bands depend sensitively on the nature of surface defects, which are the dominant source of stress and subsequent deformation inhomogeneity.

Thinning instability and adiabatic shear deformation can cooperate in a more complex serial failure process. Thinning instability can initiate when saturation of plastic strain hardening is overcome by the thinning geometric softening. Adiabatic deformation inhomogeneities brought about during growth of the thinning region can, in turn, trigger local adiabatic shear deformation and complete the failure process.

Plastic thinning instability and localization of adiabatic shear deformation are potential contributions to the processes of failure and rupture of dynamically expanding metal shells. Neither mechanism, however, is either complete, or necessary to the breakup process. Rupture ultimately requires the breaking of molecular bonds and the development of damage within the deforming material. In the fracture of metal this process has been shown to require a level of plastic deformation combined with a state of tensile stress triaxiality. This underlying physics has been noted from at least the early works of Mott [Mott, 1948] and has been addressed in considerable detail by later workers [e.g., Hancock and Mackenzie, 1976]. This feature of fracture is recognized, but will not be pursued in detail in the present development of a failure criterion.

6.3.1 Biaxial Strain Fracture Criterion

A theory and analytic model appropriate to the present dynamic fragmentation of biaxial expanding ductile shells is sought to predict the onset of fracture of a generally biaxial stretching sheet element of metal as illustrated in Fig. 6.9. Plastic stretching is brought about by an outward expansion velocity

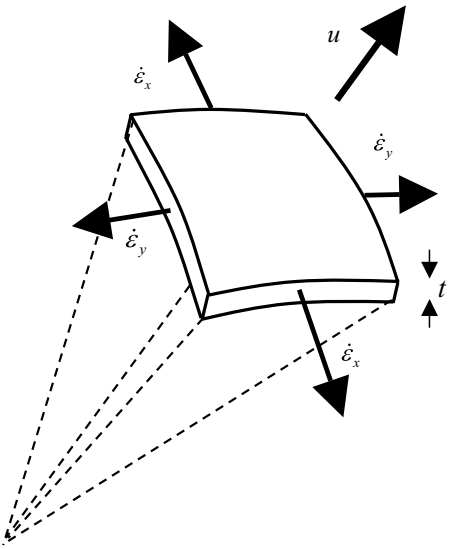

Fig. 6.9. Biaxial expanding element of metal plate with current thickness t due to imparted outward velocity u. Principal in-plane plastic stretching rates are identified

u imparted to the body. Current thickness of the element is t, while in-plane principal stretching rates are $\dot{\varepsilon}_x$ and $\dot{\varepsilon}_y$, respectively. Equivalent plastic strain rate in the element is provided through the relation,

$$\dot{\bar{\varepsilon}} = \sqrt{\frac{2}{9}\left[\left(\dot{\varepsilon}_x - \dot{\varepsilon}_y\right)^2 + \left(\dot{\varepsilon}_y - \dot{\varepsilon}_z\right)^2 + \left(\dot{\varepsilon}_z - \dot{\varepsilon}_x\right)^2\right]} \ . \tag{6.26}$$

Through-the-thickness stretching rate $\dot{\varepsilon}_z$ is related to the current thickness t of the element through the relation $\dot{\varepsilon}_z = \dot{t}/t$. The present problem is adequately addressed by considering motions characterized by the constant proportionality α of the in-plane stretching rates,

$$\alpha = \dot{\varepsilon}_y / \dot{\varepsilon}_x \ . \tag{6.27}$$

Special cases, of course, include spherical, or equiaxial, expansion ($\alpha = 1$), uniaxial cylindrical expansion ($\alpha = 0$), and the expanding ring ($\alpha = -1/2$).

Combining (6.26) and (6.27), along with the incompressibility condition,

$$\dot{\varepsilon}_x + \dot{\varepsilon}_y + \dot{\varepsilon}_z = 0 \ , \tag{6.28}$$

yields,

$$\dot{\bar{\varepsilon}} = -\sqrt{\frac{4}{3}\frac{\left(1 + \alpha + \alpha^2\right)}{(1+\alpha)^2}}\dot{\varepsilon}_z \ . \tag{6.29}$$

Equivalent plastic strain rates relative to the thinning rate and expansion rate as a function of α are illustrated in Fig. 6.10.

The plane stress ($\sigma_z = 0$), effective stress is provided by,

$$\bar{\sigma} = \sqrt{\sigma_x^2 + \sigma_y^2 - \sigma_x \sigma_y} \ , \tag{6.30}$$

where σ_x and σ_y are the in-plane principal stresses. In the present development stresses and strains are thickness averages through the sheet and only in-plane stresses are non-zero. For the corresponding proportional loading to the elastic limit,

$$\sigma_x = E\frac{1 + \alpha\nu}{1 - \nu^2}\varepsilon_x \ , \tag{6.31}$$

$$\sigma_y = E\frac{\alpha + \nu}{1 - \nu^2}\varepsilon_x \ , \tag{6.32}$$

where E is Young's modulus and ν is Poisson's ratio. The stress ratio is then,

$$\frac{\sigma_y}{\sigma_x} = \frac{\alpha + \nu}{1 + \alpha\nu} \ . \tag{6.33}$$

For a von Mises yield condition,

$$\sigma_x = \frac{Y}{\sqrt{1 - \beta + \beta^2}} \ , \tag{6.34}$$

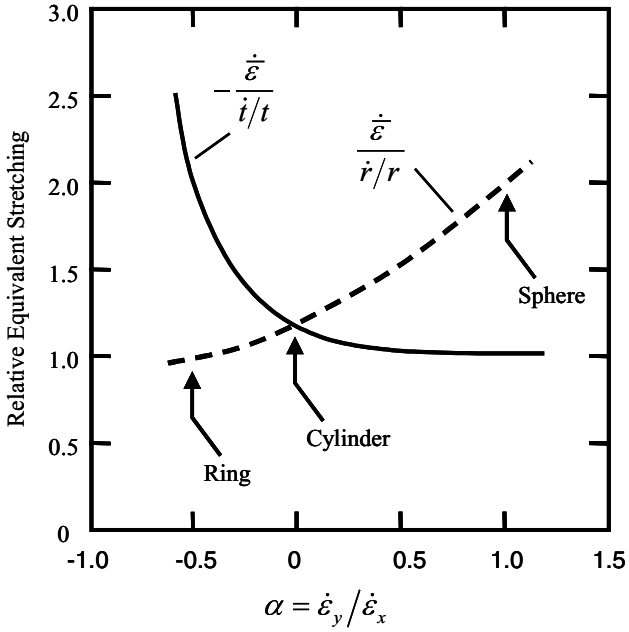

Fig. 6.10. The ratio of equivalent plastic stretching rate to the thinning rate is shown by the *solid curve*. The ratio to the expansion rate is provided by the broken curve. Values for expanding ring, expanding sphere and a uniaxial expanding cylinder geometries are identified

$$\sigma_y = \frac{\beta Y}{\sqrt{1-\beta+\beta^2}} \,, \tag{6.35}$$

where, Y is the yield stress and β is the stress ratio in (6.33). Equation (6.30) for a von Mises material gives $\bar{\sigma} = Y$.

A power-law hardening representation for the adiabatic effective stress versus strain behavior of the material of concern will be assumed of the form,

$$\bar{\sigma} = A\bar{\varepsilon}^n \,, \tag{6.36}$$

where both the coefficient A and the exponent n may, in general, depend on the biaxial proportionality parameter α. An effective in-plane tension T is provided by the product of the effective stress and the current thickness,

$$T = \bar{\sigma} t = A\bar{\varepsilon}^n t \,. \tag{6.37}$$

In the present model, onset of fracture is assumed to occur according to a maximum load instability criterion; namely, when the tension $T(\bar{\varepsilon})$ achieves a maximum under the proportional deformation loading. This instability criterion has been found to satisfactorily reproduce results of more detailed stability analyses [e.g., Romero, 1991]. The maximum of $T(\bar{\varepsilon})$ is identified from the differential,

$$dT = nA\bar{\varepsilon}^{n-1}td\bar{\varepsilon} + A\bar{\varepsilon}^n dt \ . \tag{6.38}$$

From (6.29),

$$\bar{\varepsilon} = -f(\alpha)\varepsilon_z \ , \tag{6.39}$$

where, $f(\alpha)$ is identified in the equation and,

$$d\bar{\varepsilon} = -f(\alpha)d\varepsilon_z = -f(\alpha)dt/t \ . \tag{6.40}$$

Combining (6.38) and (6.40), and equating the differential to zero, yields for the fracture criterion the critical effective fracture strain,

$$\bar{\varepsilon}_f = f(\alpha)n(\alpha) = \sqrt{\frac{4}{3}\frac{(1+\alpha+\alpha^2)}{(1+\alpha)^2}}n(\alpha) \ , \tag{6.41}$$

where the possible dependence of n on the biaxial proportionality parameter α is noted. Identifying through-the-thickness strain as $\varepsilon_z = \ln t/t_o$ thinning at fracture is,

$$\frac{t_f}{t_o} = e^{-n(\alpha)} \ . \tag{6.42}$$

Zero plastic volume strain for proportional loading of the familiar geometries requires that,

$$r_f t_f^{\kappa(\alpha)} = r_o t_o^{\kappa(\alpha)} \ , \tag{6.43}$$

where, $\kappa(\alpha) = 1/2,\ 1$, and 2 for an expanding sphere, uniaxial cylinder, and expanding ring geometry, respectively. The radial expansion at failure is then,

$$\frac{r_f}{r_o} = e^{\kappa(\alpha)n(\alpha)} \ . \tag{6.44}$$

In the absence of further data it is sensible to propose that the power-law hardening coefficient n in (6.36) be independent of the proportionality parameter α. The expanding ring data for U6Nb [Grady and Olsen, 2003] then provide a measure of the coefficient n for the dynamic expansion and fracture of the ductile uranium alloy. The data of Olsen indicate that $r_f/r_o \cong 1.3$ and (6.44) provides $n \simeq 0.13$.

Based on a power law hardening exponent of $n \simeq 0.13$ for the uranium alloy U6Nb, the through-the-thickness thinning, radial expansion, and equivalent plastic strain is shown in Fig. 6.11 as a function of the biaxial stretching parameter α. It is notable that both expansion and equivalent plastic strain reduce markedly as biaxial deformation approaches cylindrical, and then spherical, expansion.

Concerning the load maximum localization and fracture criterion, it has been noted [e.g., Storen and Rice, 1975; Needleman and Tvergaard, 1992] that only for $\alpha \leq 0$ is there a line of zero extension determining the orientation of the thinning localization. For $\alpha > 0$ a line of zero extension does not exist. Nonetheless, deformation localization when both in-plane principal strains are

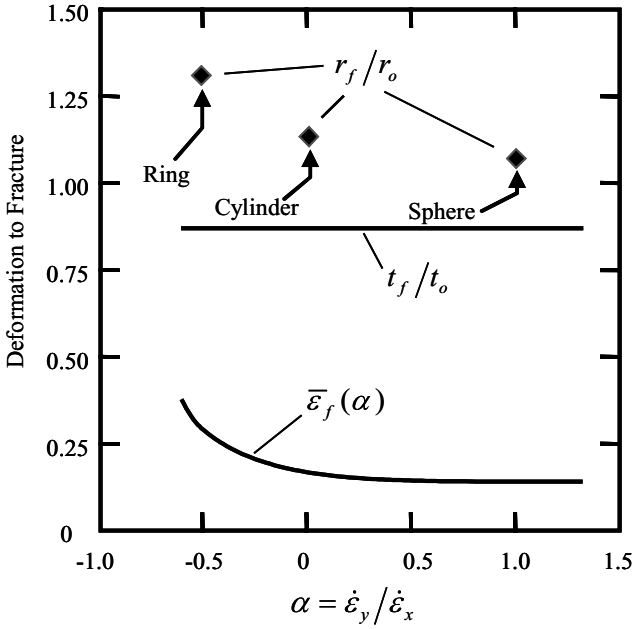

Fig. 6.11. Equivalent strain, thinning and radial expansion at fracture onset for U6Nb uranium alloy based on a power law hardening and load maximum model

positive is observed. Romero (1991) has demonstrated instability of the Levy-von Mises equations of a biaxial stretching ($\alpha = 0$) perfectly plastic plate, providing some justification of the load maximum criterion outlined here.

The power law hardening relation in (6.36) might be expected to depend on the biaxial load path α if deformation softening due to growth of microvoid damage in turn depended on the state of stress triaxiality [e.g., Mott, 1948; Hancock and MacKenzie, 1976]. Stress triaxiality equals 1/3 for $\alpha = -1/2$ and 2/3 for $\alpha = 1$. Additional test data would, of course, be needed to assess such load path dependence.

References

Abramowitz, M. and I. A. Stegun, eds. (1954), Handbook of Mathematical Function, No. 55, *National Bureau of Standards Applied Mathematics Series*, U. S. Government Printing Office.

Barlat, F. (1989), Forming Limit Diagrams – Predictions Based on Some Microstructural Aspects of Materials, in Form Limit Diagrams: Concepts, Methods and Applications, R. H. Wagner, K. S. Chang, S. P. Keeler, eds., The Minerals, Metals & Materials Society.

Buck, R. C. (1965), Advanced Calculus, McGraw-Hill, New York.

Grady, D. E. and Olsen, M. L. (2003), A Statistical and Energy Based Theory of Dynamic Fragmentation, *Int. J. Eng. Mech.*, 29, 293–306.

Gurney, R. W. (1943), The Initial Velocity of Fragments from Bombs, Shells and Grenades, Army Ballistic Research Laboratory Report BRL 405.

Hancock, J. W., and Mackenzie, A. C. (1976), On the Mechanisms of Ductile Failure in High-Strength Steels Subjected to Multi-Axial Stress States, *J. Mech. Phys. Solids*, 24, 147–169.

Needlemann, A., and V. Tvergaard (1992), Analysis of Plastic Flow Localization in Metals, *Applied Mechanics Review*, 45, s3–s18.

Mott, N. F. (1948), Fracture of Metals: Theoretical Considerations, *Engineering*, 165, 16–18.

Romero, L. A. (1991), The Stability of Stretching and Accelerating Plastic Sheets I & II, *J. Appl. Phys.* 69, 7474–7486, 7487–7499.

Storen, S. and J. R. Rice (1975), Localized Necking in Thin Sheets, *J. Mech. Phys. Solids*, 23, 421–441.